INSTITUTE OF PHYSICS PUBLISHING MEASUREMENT SCIENCE AND TECHNOLOGY
Meas. Sci. Technol. **13** (2002) 997–1005 PII: S0957-0233(02)31367-5

Measurement of digital particle image velocimetry precision using electro-optically created particle-image displacements

Marcus Megerle[1], **Volker Sick**[2,4] **and David L Reuss**[3]

[1] Sandia National Laboratories, Combustion Research Facility, MS-9053, PO Box 969, Livermore, CA 94551-0969, USA
[2] Department of Mechanical Engineering, The University of Michigan, 2202 GG Brown Building, 2350 Hayward Street, Ann Arbor, MI 48109-2125, USA
[3] General Motors R&D Center, 30500 Mound Road 106, Mail Code 480-106-252, Warren, MI 48090-9055, USA

E-mail: mvmeger@sandia.gov, vsick@umich.edu and david.l.reuss@gm.com

Received 29 November 2001, in final form 4 March 2002, accepted for publication 14 March 2002
Published 20 June 2002
Online at stacks.iop.org/MST/13/997

Abstract
The displacement (velocity) precision achieved with digital particle image velocimetry (PIV) was measured. The purpose of this work was to determine the precision and sensitivity of digital PIV using real rather than theoretical images at 1 and 2 mm spatial resolution. The displacement measurement precision was determined by measuring the RMS noise from 60 identical displacement distributions. This work is unique in that it uses electro-optical image shifting to create a repeatable image displacement distribution of random particle fields. The displacement variance between images is caused by the shot-to-shot variation in: (1) the particle-image fields, (2) the camera noise and (3) the variance in the correlation peak detection. In addition to magnification variations, the particle-number density, imaging-lens f-stop and image-plane position errors were varied to determine the best configuration. The results indicate that both the ensemble-mean and the RMS fluctuations of the image displacements are affected by these parameters and comparisons with results found in the literature are presented. The extents of these variations are quantified. This variance does not, of course, include errors due to random gradients and out-of-plane pairing losses, which exist in real turbulent flows.

Keywords: digital particle image velocimetry, measurement precision, measurement uncertainty

(Some figures in this article are in colour only in the electronic version)

1. Introduction

Application of particle image velocimetry (PIV) for quantitative turbulence measurements requires knowledge of the accuracy and precision that can be achieved. Furthermore, it is of practical interest to quantify the extent to which variations in the experimental setup parameters affect the accuracy and precision. The goal of this study is to quantify the influence of particle number density, the f-number of the imaging system, focusing errors and magnification on the measurement accuracy and precision. Most previous work has addressed such issues from a theoretical point of view. Keane and Adrian (1990) conducted Monte Carlo simulations aimed at optimizing PIV-system parameters

[4] Author to whom any correspondence should be addressed.

with photographic recording in mind, which was more practical at the time; consequently, autocorrelation on an interrogation spot of 256 × 256 pixels was employed. Data validation criteria, particle image density, relative in-plane image displacement, relative out-of-plane image displacement, velocity gradient parameter and the ratio of the mean image diameter to the interrogation spot size diameter were evaluated. Some of the assumptions limit direct comparisons with current experimental PIV employing digital (CCD) recording practices. In particular, CCD recordings often use interrogation windows that are 32 × 32 (or less) pixels in size and fewer pixels to resolve the particle images (Raffel *et al* 1998). To address CCD recording, Adrian (1997) performed simulations of PIV for maximizing the dynamic ranges of space and velocity, while simultaneously conducting accurate, low-noise measurements. Guidelines for optimum usage of size-limited CCD arrays were given to maximize the field-of-view while not losing necessary particle image information for accurate detection. The influence of irregularly shaped particle images that arise as a consequence of noise in the light field, such as background speckle, aberrations of lenses, noise of the image recording medium, electronic noise in circuits, shot-to-shot noise in the photo detection process, root mean square (RMS) error in determining the displacement of the centroid of the particle image was referred to but not evaluated. It was recommended that one should record a particle image that is 1–3 times the size of a pixel (generally twice the size) to avoid errors due to finite resolution. This in turn determines the maximum field-of-view by the available size of the CCD array. A procedure is outlined to trim the system to best usage by selecting the optimum magnification as well as f-number.

Westerweel (1997) simulated digital PIV in terms of linear system theory to optimize and improve the measurement performance. Autocorrelation in conjunction with Monte Carlo simulations and experimental test measurements from the literature were employed. Modelled optics consisted of aberration-free circular lenses with a numerical aperture $f/\#$, and all observed particles were in focus. The chosen optimization criteria were based on maximization of the height of the displacement correlation peak R_D with respect to the random correlation. Problems inherent to pixelization as a consequence of a digital recording were addressed and discussed thoroughly. Emphasis was given to the fact that the measurement resolution is determined by the ratio of particle image size and interrogation spot size and not the ratio of pixel size to interrogation spot size. More than two pixels for recording the particle image seems unnecessary in terms of the trade-off leading to a reduction in the size of the field-of-view. Sub-pixel resolution can be achieved if the correlation peak covers more than one pixel and is independent of the actual particle image size. When the ratio of the particle image diameter to the pixel size is small (i.e. between 1 and 2) the diameter of the correlation peak is limited to three pixels that are above the background noise.

An experimental study performed by Willert and Gharib (1991) used simulated particles (a random pattern of black dots on a white background) to study the effect of particle image number densities on the accuracy of the measurements. The black-dot target was mounted on a linear translation stage and imaged with varying offsets (particle image displacements) between the first and second exposures. These images are idealized in that they do not produce particle images with varying intensities, irregular shapes and varying image sizes. In a later experimental study Willert (1996) investigated the measurement uncertainty of actual photographic PIV recordings as a function of various parameters when the recorded negatives are digitized by means of a scanner in a post-processing step. Parameters considered for the digital evaluation of the photographic recordings are the image depth, the interrogation window size, the displacement magnitude between the first and second exposure and image offset between the correlation windows. Quantitative uncertainty is experimentally obtained by imaging real particles in a stagnant flow with an artificial displacement achieved by means of a rotating mirror positioned in the image-recording path, comparable in concept to this study. The measurement uncertainty was evaluated based on an individual double-exposed image, where a least-squares fit was calculated to present an artificial mean and the measurement uncertainty was expressed as the variance of the instantaneous vector field. However, the error contribution of the least-square fit is not quantified and no statements regarding the variability of the image shifting technique and the inhomogeneity of the displacement field are provided. In contrast, this study obtains the ensemble mean by averaging 60 exposures and the RMS is evaluated at each spatial point in the field as variance with respect to the local mean. There are two apparent differences. Willert did not address the question of repeatability (image-to-image variation) of the measured results and secondly the RMS relies on regional homogeneity in displacement as the mean is based on a least-square fit. In the present study, inhomogeneities in displacement cancel out as for each spatial location the ensemble mean provides a value independent of the neighbouring vectors. Willert (1996) also demonstrated that smaller values of the ratio of the particle image diameter to the pixel size result in a bias error known as pixel locking. Westerweel (2000) states three conditions that do not lead to a bias caused by pixel locking and that are relevant to the current study where no pixel locking was observed. Pixel locking is not relevant if: (1) the ratio of particle image size to pixel size is 2 or higher, (2) if a spatial offset between the two interrogation windows is used in the correlation and (3) if the number of particle images contained in the second interrogation spot is close to that of the first window. The particle image size criterion is not satisfied for the range found in this study, where image diameters between 1.3 and 1.8 pixels were observed and pixel locking cannot *a priori* be ruled out. However, conditions (2) and (3) were satisfied in this study. Consequently, as the last two conditions are satisfied in this study, pixel locking is not expected and is indeed not found to have an impact on displacement inaccuracy. However, this fact lacks experimental generalization as no integer value displacement was encountered under the chosen parameters. Furthermore, it was found that the measurement precision, determined by the ratio of particle image size to interrogation spot size, is independent of the seeding density (Westerweel 1997).

This study and that of Willert (1996) follow a similar approach and they will be compared when appropriate. In addition to the experiments, Willert (1996) employed Monte

Carlo simulations to investigate other parameter influences on measurement uncertainties he could not readily vary independently in the experiments, such as seeding density, offset of the interrogation window and particle image diameter. The work presented here experimentally investigates the influence of seeding density, f-stop, magnification and defocusing on the measurement precision and accuracy of digital PIV using real particles. Correlation parameters (interrogation window size, offset) were examined initially and then fixed for this analysis. The usual problem with real particles is that the flow field needed to create the displacement is unknown; consequently, the measured precision is a combination of uncertainty in both the flow and PIV interrogation technique. This problem is overcome here using electro-optical image shifting introduced by Landreth and Adrian (1988). The technique was developed to solve problems associated with directional ambiguity in PIV measurements when using auto-correlation on double-exposed images. With this method, the particles are imaged through a birefringent crystal, thereby creating a repeatable displacement on top of the displacement given by the flow. The method requires the use of cross-polarized laser sheets for particle illumination.

2. Experiment

2.1. Electro-optical image shifting

Electro-optical image shifting is the foundation for this experimental study of PIV precision. It was originally introduced to overcome the directional ambiguity in PIV measurements using doubly exposed images and autocorrelation (Landreth and Adrian 1988) by introducing a fixed (known) shift between the two exposures. For this study, it is used because there is no image-to-image variation in the displacement distribution in an otherwise stagnant flow situation. Briefly, the particles are illuminated with cross-polarized laser sheets and viewed by the lens through a birefringent crystal. Each particle is thereby recorded as two images, one from each polarization, as illustrated in figure 1. A distribution of particle displacements results as described in Landreth and Adrian (1988) and depicted in figure 2. Thus, if one considers a particular location within the field-of-view, an individual particle will always result in the same displacement vector between a pair of particle images in the recording plane. In this study, a 3 mm thick calcite crystal was used to induce the electro-optical image shift. The crystal axis was cut as described in Reuss (1993) and the crystal was placed in front of the imaging lens.

In contrast to simulation-based studies, this experimental approach includes real noise sources, such as those acknowledged by Adrian (1997) and Willert (1996), and tests their influence on the overall performance of the acquisition system as well as the PIV algorithm. These noise sources can be attributed to irregularities in the shape of particle images caused by non-homogeneous illumination within the laser light sheets, partly due to background speckle, and aberrations induced by real imaging lenses and lens groups. In addition to these sources of noise, electronic noise in circuits and shot-to-shot noise in photon detection processes involved with the CCD camera are included in the experiment. Also, noise arises from the RMS error inevitable in determining the location of displacement of the particle image. One can disregard the influence of uncertainty in the time separation between exposures as flow is nearly stagnant and both laser sheets are triggered with no time separation (see what follows).

2.2. Experimental hardware

The experimental test section was a cube (dimensions 180 mm) with flat, transparent walls for optical access of the laser sheet and camera as well as mechanical access for seeding, evacuating and mixing to homogenize the seed distribution. The flat quartz windows (thickness 2.5 mm) did not introduce noticeable aberration and can consequently be treated as a simple containment for the seeded air rather than an optical element. All measurements were conducted at ambient pressure, temperature and quiescent flow conditions. Schematically, the test section is shown as the insert in figure 1 with the laser light sheet and the signal directions indicated.

A six-jet atomizer (TSI model 9306A) was employed to generate silicone oil droplets with 1 μm diameter. The particles were introduced into the chamber through a tube with a perforated disc at its end. This round disc covered about 80 mm in cross section and served as a mixer to homogenize the seed density inside the chamber. The disc could be moved along an axis aligned in the plane of the laser sheets at half-height of the area of interest to assist mixing and to eliminate the occurrence of random air pockets of lower seed density. The seed density was iteratively adjusted by adding dilution air and was determined by counting the number of particles within the size of the interrogation spot being tested (32×32 pixels). The seeded air was allowed to settle to a nearly quiescent, homogeneous distribution of particles of the desired seeding density before each test. Contamination of the test section windows with the dispersed particles was found to be minimal and due to the fact that the laser sheet was at a distance to the windows (approximately 40 mm) well outside the depth of focus, no deterioration in the imaging quality was observed. A data set taken at a particular setting contains 60 individual realizations recorded within 30 s. During this period a slow migration of the overall particle pattern due to the mixing process and buoyancy could be observed, with an estimated maximum progression of flow structures at less than 1 cm s^{-1}. However, note that the measurements are completely immune to this slow flow because both lasers were fired at the same time. Thus, the only shift that is measured as a displacement between particle images is given by the properties of the birefringent crystal.

The laser sheet was created from a dual-cavity Nd:YAG laser at 532 nm. The two beams were cross polarized as required to create the electro-optically induced image shift (see Landreth and Adrian 1988). The lasers were Q-switched simultaneously. Thus, displacement due to flow is eliminated and only the electro-optical displacement is recorded by the camera. Laser power levels were adjusted to the parameter cases investigated in order to maintain a constant illumination level of the particles, where only the brightest particle images were allowed to result in an intensity saturation of the CCD sensor. This was achieved by adjusting the Q-switch timing with respect to lamp firing timing to yield power levels per

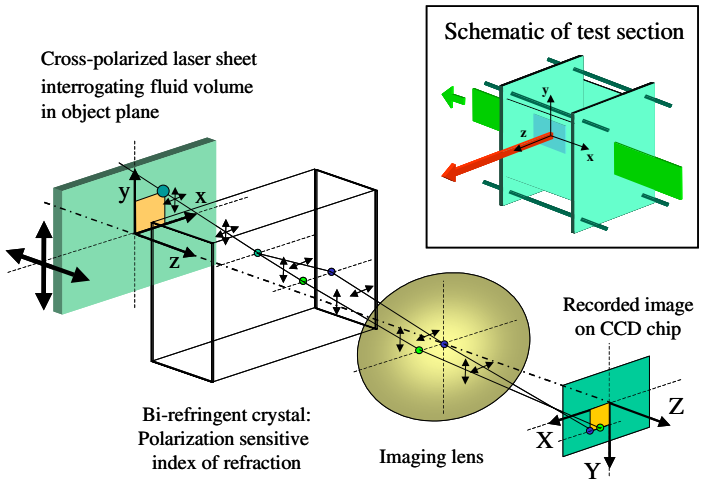

Figure 1. Schematic of the experimental setup and the electro-optical image shifting technique. The inset shows the test section, the location of the cross-polarized laser sheets (at $z = 0$) and the direction towards the camera (in the positive z-direction).

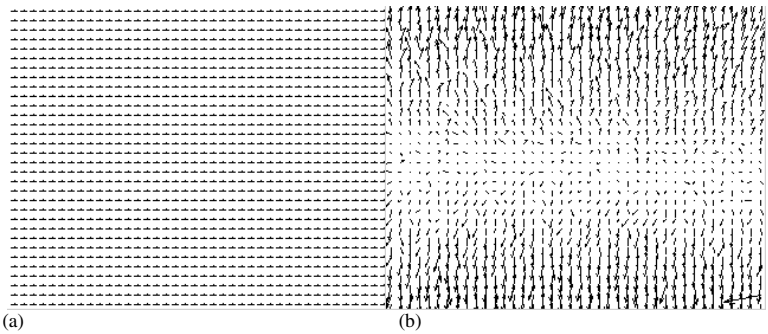

Figure 2. Ensemble-averaged velocity distribution (*a*), and after subtraction of the spatially integrated mean velocity field (*b*), at $M = 0.107$ and $f/\# = 8$. Note that the displacement vector representation is a factor of 100 larger in (*b*) as compared to (*a*), where the horizontal mean displacement is 3.902 pixels; every second vector is shown. The pattern in (*b*) reflects a combination of both a systematic spatial variation due to the birefringent crystal and an inevitable random RMS noise.

beam from time integrated values of about 250 mW at $f/8$ to 30 mW at $f/2.8$ for a pulse frequency of 10 Hz.

A Nikon MicroNikor ED 105 mm focal length lens was used at fixed magnifications and the camera translated to find the focal position. The camera (for specifications, see table 1) was positioned using a micrometer-controlled xyz-translation stage as well as a rotation and tilt stage. Magnifications of $M = 0.107$ and 0.214 were used resulting in fields-of-view of 64×80 and 32×40 mm, respectively. The values for M were chosen as representative for targeted measurements in optical engines. The specific values of magnifications for the optical recording system were experimentally determined by means of imaging a reference grid with 1 mm line spacing located in the object plane at best focal distance. As the chip size is known in terms of geometric size as well as in terms of the number of pixels and their dimensions in each coordinate direction, the magnification can be adjusted as the camera distance is varied in respect to the object plane while the number of pixels representing a given distance on the imaged grid are evaluated until the desired magnification is achieved (e.g. to achieve a magnification of $M = 0.107$, 5 mm of grid in object space are recorded onto 80 pixels in the image plane (chip), each pixel being 6.7 μm wide, consequently spanning over a distance of 0.536 mm).

2.3. Procedures

The birefringent crystal was rotated such that its optical axis orientation resulted in a displacement vector that was characterized by a large horizontal component with a very small component in the vertical direction. The vertical displacement vector was typically less than 0.1 pixels or about two orders of magnitude smaller than the horizontal component. Horizontal shifts between the peaks of corresponding image pair partners of about 8–9 pixels for $M = 0.214$ and approximately four pixels for $M = 0.107$ were found by visual inspection of the images. A quasi-cross-correlation algorithm was then used to evaluate the particle displacement of double-exposed image fields, which used a spatial offset equal to the image shift that was found by visual inspection. An interrogation window offset equal to the average displacement will result in the smallest error arising from the correlation process if a double-exposed image is employed as also shown experimentally via a simulation by Willert (1996). The allowed vector length range was set to $\pm 25\%$ of the initial shift. Results were the same for a 50% range as no outliers were detected.

The interrogation-spot size was chosen as 32×32 pixels for all cases. Using a 50% overlap of the interrogation areas resulted in vector grid spacings of 0.5 and 1 mm,

Table 1. The technical specifications of the CCD camera.

Camera	LaVision Inc., FlowMaster FM 3S
Chipset	Sony INTERLINE 2/3 SVGA progressive scan with 'lens-on-chip'
Dynamic range (bit)	12
Readout	Non-interlaced, full field readout @ 12.5 MHz
Readout noise	<2 counts (<8 e^-) RMS @ 12.5 MHz
Camera cooling system	2 stage TE with forced air regulated to $-12\,^\circ$C
Size of CCD sensor (px)	1024×1280
Pixel size (μm px^{-1})	6.7×6.7

with spatial resolutions of 1 and 2 mm, respectively, for the two magnifications $M = 0.214$ and 0.107. These spatial resolutions are based on independent (i.e. non-overlapping) vector measurements within the actual interrogation-spot size of 32×32 pixels, as each vector is based on the correlation of data contained within this area. The fact that a denser grid of vectors can be generated by employing a 50% overlap does not change the resolution of the flow but acts rather as a low-pass filter, since a fraction of the same data is used a multiple of times for calculating the displacement vector in adjacent cells. Before processing the images, a sliding background (high-pass filter) with a scale length of 15 pixels was subtracted from the images to increase the contrast of the individual particle images. This technique searches for the minimum intensity value in an array of 15×15 pixels in size, centred over the respective pixel to be corrected and subtracts the lowest found pixel intensity from the actual value to enhance contrast and minimize the effect of possible light sheet inhomogeneities across the field-of-view. The corrected images have a lower background noise and allow improved particle detection. No post-processing other than a validation criterion based on the mean as described in the following was performed before analysing the resulting vector (displacement) fields. The validation employed compared the magnitude of each vector (for each coordinate) with the mean displacement vector and rejected without replacement if their magnitude differed by more than 25% of the mean displacement vector. The typical rejection was less than 0.1% of the total vectors mainly due to edge outliers.

For each of the experimental settings that will be described, sets of 60 individual vector fields each containing 5120 vectors were evaluated. The findings are discussed in the context of spatial and ensemble variations of shifts. Systematic variations of the measured pixel shift are expected (Landreth and Adrian 1988) that are introduced by the properties of the birefringent crystal. This is seen in figure 2 for an ensemble-averaged displacement field where two images are presented. Figure 2(a) depicts a mean displacement field obtained by ensemble averaging 60 individual realizations. The average displacement vector (ensemble and spatially averaged) is 3.900 pixels in the horizontal direction and 0.025 pixels in the vertical direction. The ensemble-averaged distribution after subtracting the average displacement vector found in (a) is presented in figure 2(b), where vector arrow lengths are multiplied by a factor of 100 to reveal the minuscule but systematic variation in displacement vector which is a known property of the crystal employed. This was discussed by Landreth and Adrian (1988) and later verified by Reuss (1993). A vector equal in length to (a) now represents a vector of 0.039 pixels length. Note, that the variation induced by the crystal is dominant in the vertical direction, whereas all results presented in this study are concerned with the error in displacement in the horizontal direction which is aligned with the mean displacement vector. Moreover, it is stressed here that any variation or local inhomogeneity in the crystal structure resulting in a characteristic spatial displacement is self-correcting in this analysis as all results are relative to the ensemble mean (as crystal properties do not change over the time intervals considered) and will hence not cause an error contribution. Depending on magnification, f-stop and defocusing this spatial variation changes but is generally found to be between 0.3 and 1.5% of the mean displacement.

In the assessment of the precision, i.e. the variation of the measured displacement over the entire ensemble of data, this variation is eliminated. The RMS of the displacements δx is determined as follows:

$$\mathrm{RMS}\,\delta x = \frac{1}{IJ}\sum_i\sum_j\left(\frac{1}{N}\sum_n(\delta x_{ijn} - \overline{\delta x_{ijn}})^2\right)^{1/2}$$

where i and j are the grid indices and n is the image number.

This ensemble RMS is computed for each individual position at locations ij before spatially averaging to the number that will be reported in the figures that follow. Thus, the systematic variations of δx caused by the crystal are eliminated.

3. Results

The reported data is given in percentages of the mean displacement for the given conditions in all graphs except figures 8 and 9. Justification for this presentation in relative values is based on results presented in figure 8 where the absolute displacement inaccuracy measured in units of pixels demonstrates a linear dependence of displacement inaccuracy on the actual displacement. This functional dependence is found experimentally in this study as well as theoretically and simulation based in Westerweel (1997). Since this dependence is commonly accepted, it was chosen for the other figures to normalize the displacement inaccuracy by the mean displacement in order to focus the attention on the effects associated with variation of other parameters rather than that due to the displacement magnitude (equal in this study to change of magnification). Note that the constant of linearity is found close to unity, and normalization by the mean displacement value is chosen for practical reasons to not distract from other trends. The range of mean displacement

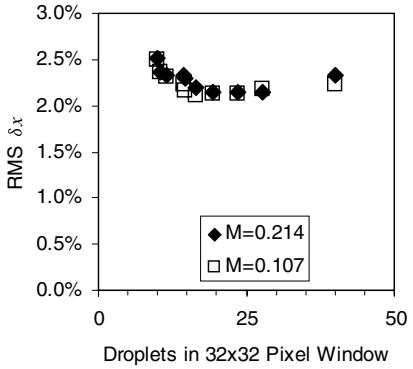

Figure 3. Variation of measured displacements for two magnifications. The f-stop was set to $f/8$ for both series. The RMS is given as a percentage of the local average displacement, which had a spatial variation of 3.894 ± 0.009 for $M = 0.107$, and 8.779 ± 0.005 for $M = 0.214$.

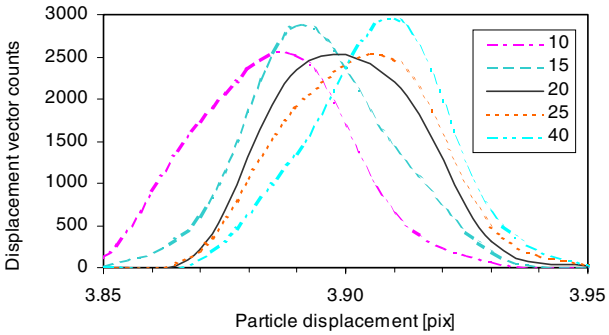

Figure 4. PDFs of the measured pixel displacement for $M = 0.107$ and varying particle seeding density (values are approximate).

values used for normalization is indicated in the respective figure caption.

The seeding density was investigated first to define a suitable operating point for the rest of the tests. For higher droplet image number densities (>20) it was difficult to count the actual number of droplet images in the 32 × 32 pixel interrogation window as the distinction between individual particle images was not unambiguous. The numbers given in figure 3 are therefore to be taken as approximate, at least for values greater than 20. For the two magnifications under study the RMS displacement is essentially independent of the droplet image density for the investigated range from about 10 to 40 droplet images in the interrogation window with a preference to densities between 20 and 30 particle images equalling particle image pairs of 10–15. This trend is in agreement with Willert (1996) and Westerweel (2000) where it is shown that after an initial strong dependence of error on seed density for low seeding densities (<5), there is a transition range of moderate dependence before for seeding densities in excess of 15 particle image pairs the error is insensitive to seeding density and the error remains essentially constant. Undoubtedly, lack of reliability of the measurement accuracy is dominating for low seeding densities (less than ten particle image pairs) and accounts for the majority of the error. For seeding densities higher than ten particle image pairs per interrogation spot, sufficient information for determining the fairly homogeneous displacement field is provided and an increase in seeding density does not deliver any new information that could lead to higher accuracy. The displacement vectors become redundant and the measurement accuracy cannot be improved upon any further. The remaining level of error, which is insensitive to an increase in seeding density, can be attributed to lack in precision alone. Consequently, the higher level in error at lower seeding densities is a combination of this error level attributable to lack of precision and a superimposed level of error due to lack of measurement reliability, as too few measurements of the displacement are available for a statistically well supported value.

The PDFs depicted in figure 4 show the measured distribution of image displacement vectors in the ensemble-averaged image for a variety of seeding densities at $M = 0.107$. The bin width was selected to be 0.005 and 0.02 pixels (only the 0.02 pixels case is displayed here for clarity) or roughly 0.1 and 0.4% of the average particle image displacement. A smooth transition of the distribution from highly seeded to low seeded cases can be observed yielding corresponding average displacement values from high to low. This trend is unaltered in both bin width examinations. The interesting feature observed is that distributions start out being skewed towards the high displacement for high density, transiting smoothly through a symmetric shape at medium density before skewing to the low displacement when reaching the low-density cases. The most symmetric PDFs correspond with the lowest RMS fluctuations. The reason for this change in the shift in the peak position and the skewness is uncertain at this time. However, the mean displacement varies on the order of 1% of the total displacement and is therefore not significant. This insensitivity of the measured fluctuations over a broad range of droplet densities simplified the assessment of the influence of the remaining parameters. Thus, seeding densities that produced 10–15 image pairs in a 32 × 32 pixel window were used for the remaining tests.

Following the principle established by Westerweel (1997) and Adrian (1997), particle images should be two to three pixels in diameter on the recording medium equal to an e^{-2}-diameter of roughly 1.5–2.0 pixels. The particle image diameters are deduced from an analysis of the self-correlation peak diameter which is $2^{0.5}$ times the magnitude of the diameter of the average particle image diameter in the interrogation spot size used for the auto-correlation (Keane and Adrian 1990, Westerweel 1997). To obtain the information about the self-correlation peak diameter it is necessary to perform a Gaussian curve fitting function along the intensity profile of the self-correlation peak and obtain its diameter, which is defined as the width of the Gaussian function at a value of e^{-2} or 13.5% of its peak height over base line. The Gaussian curve was fitted to five neighbouring pixels centred over the pixels with the highest intensity. In the experiments the location of the plane of best focus was obtained as images were continuously recorded and monitored while the distance from the camera to the object plane, i.e. the laser sheet, was varied by means of a translation stage, until the observed particle images were smallest, strongest in intensity and the initial mixing related seeding inhomogeneities prior to reaching equilibrium were best resolved visually in the image plane. In a second step, the particle image diameters were calculated according to the above method to confirm that selected locations of best focus

correlated with minimum diameters as recorded in comparison to off-focus recordings that were obtained by varying the distance from the camera to the object plane. In the remainder of this study, the term image diameter refers to the width of the intensity profile of a particle image at an e^{-2}-height.

In a real system the particle diameter is affected by the particle size, theoretical diffraction limit of the lens system, the aberrations of the lens and the care in determining the best focus. Here, the particles are much smaller in size (1 μm) than the diffraction limit and the lens system is fixed. Consequently, most of the diameter variation is due to the diffraction limit dependence on f-stop, focus and magnification. Thus, in practice the particle size can be varied by two means. First by changing the aperture, $f/\#$, and second, by selecting the image plane to be located at the distance of best focus or purposely varying this distance to achieve degraded imaging of particles that are now imaged in an out-of-focus distance and appear enlarged and less intense. In this study, the droplet image diameters were approximately 1.3 and 1.5 pixels for $M = 0.107$ and 0.214, respectively, at best focus. Moving the camera out of focus, the image size increased from 1.5 pixels at best focus to 1.9 and 2.7 pixels for 2 and 4 mm off focus, respectively ($f/5.6$ and $M = 0.214$).

The effect of the aperture on the RMS noise of the displacement is shown in figure 5. For both magnifications an optimum aperture was found, i.e. $f/4$ and $f/5.6$ for $M = 0.107$ and 0.214, respectively. The average displacements were insensitive to the variations in $f/\#$, changing by 0.7 and 0.9% of the mean for $M = 0.107$ and 0.214, respectively, over all values of $f/\#$ investigated here. Following the derivation provided by Adrian (1997) a clear increase in particle image diameter was expected for the employed particle size, magnifications and f-stops at best focus for increasing f-number, in value for $M = 0.214$ from 1.2 pixels for $f/2.8$ to 2.1 pixels for $f/8$, equal to an 80% increase in diameter. Similar values are found for $M = 0.107$ where the diameter increases by 70%. However, experimentally this effect was found to be reversed and much less pronounced with values based on the derivation of the particle image diameter from the self-correlation peak as described earlier. The results found indicated a 12 and 5% decrease in image diameter for $M = 0.214$ and 0.107, respectively from $f/2.8$ to 8. We speculate that the image size decreases with increasing $f/\#$ contrary to diffraction theory because aberrations of real lenses decrease with increasing $f/\#$.

The effect of defocusing is shown in figure 6 and demonstrates that the smallest uncertainty was always achieved with the optics aligned for best focus, i.e. smallest particle image. It is also interesting to note that the measurements show the smallest RMS δx for $M = 0.214$. Proper focusing is essential for highest precision. Especially, for $M = 0.214$, defocusing has a significant detrimental effect on the precision as the depth-of-field is roughly a third that found with $M = 0.107$ based on theory following Adrian (1997). Consequently, in the case of $M = 0.107$ the focus variations were only extending to about 80% of the depth-of-field and a linear, weak increase in measurement uncertainty is observed. In contrast, for $M = 0.214$, the second off-focus recording occurred at a distance about twice that of the depth-of-field (equivalent to 200%) in distance from the focused case and resulted in a highly nonlinear error increase compared to the first off-focus measurement which was taking place right at the distance equal to the depth-of-field. The focus offset distances were selected to serve as a compromise for both cases while keeping the actual offset distance equal for both magnifications regardless of the differing depth-of-field. Looking at the combined effect of focus and $f/\#$ in figure 6 shows that the RMS noise increases with low $f/\#$ (large aperture) and defocusing. Both of these changes reduce the imaging quality of any real image system. The small $f/\#$ (large aperture) tends to increase aberrations and thereby creates a larger, asymmetric, and lower intensity image (watts/unit area). The defocusing will further enlarge the images. This suggests that the increase in the RMS error may be a result of the increased image aberration. This hypothesis is further supported by figure 7, which shows the displacement PDFs for the range of f-numbers and best focus settings of $M = 0.107$. It can be observed that the kurtosis increases as $f/\#$ decreases from $f/5.6$ to $f/2.8$. Following this argument further, the error detecting the peak of the Gaussian fit to the displacement correlation would increase with increasing aberrations, which is intuitively reasonable.

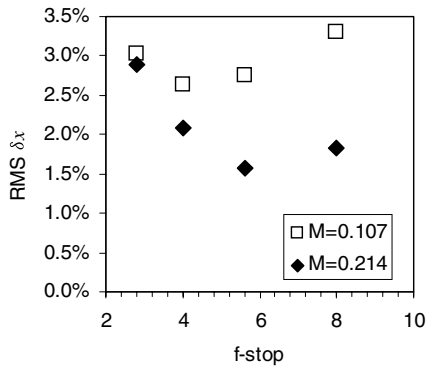

Figure 5. The selection of the f-stop has a more pronounced effect on displacement fluctuations for $M = 0.214$. The RMS is given as a percentage of the local average displacement, which had a spatial variation of 3.88 ± 0.01 for $M = 0.107$, and 8.78 ± 0.05 for $M = 0.214$.

Pixel locking effects are known to be of importance if the particle image is small relative to the pixel dimensions (<2 pixels). Pixel locking results in a displacement bias toward integer values, which might increase the overall error. Referring to figures 4 and 7, it can clearly be seen that pixel locking did not occur, as the presented PDFs contain in excess of 99.5% of all evaluated vectors and none of them is binned (bin width 0.005 pixels) onto an integer value. Explanations for this insensitivity to pixel locking can be found in Westerweel (2000) and are abstracted here. Firstly, pixel locking is known for ratios of particle image size to pixel size of 2 or less, which is around the limit of this study (see also figure 8) thus insensitivity is not surprising as the condition might lead either way. Such bias does not occur if there is, secondly, a general offset between the interrogation windows and thirdly, if the number of particle images contained in the second interrogation spot is closely comparable to that of the first window. Consequently, as the above stated conditions are satisfied in this study pixel locking is not expected and is indeed not found to have an impact on displacement inaccuracy. The case cannot be generalized from this experiment as no

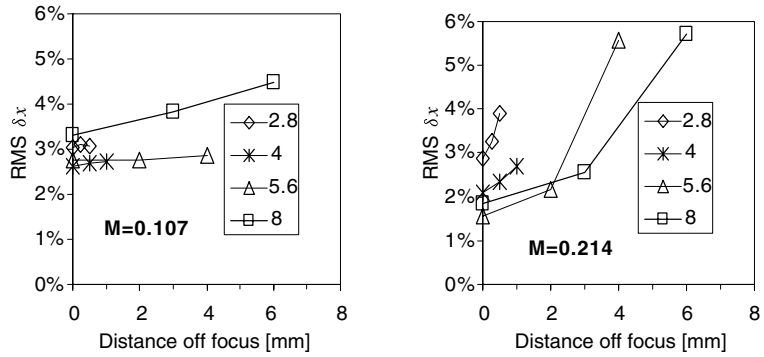

Figure 6. Defocusing has a detrimental effect on the RMS fluctuations of the measured displacement δx for all f-stop settings and magnifications that were investigated. The RMS is given as a percentage of the local average displacement, which had a spatial variation of 3.88 ± 0.01 for $M = 0.107$ and 8.70 ± 0.10 for $M = 0.214$.

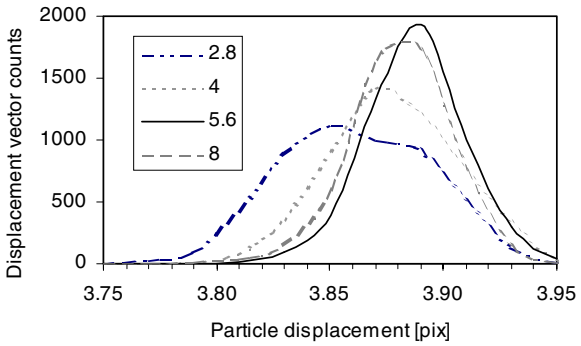

Figure 7. PDFs of the measured pixel displacement for $M = 0.107$ and the best possible focus settings for varying f-stops.

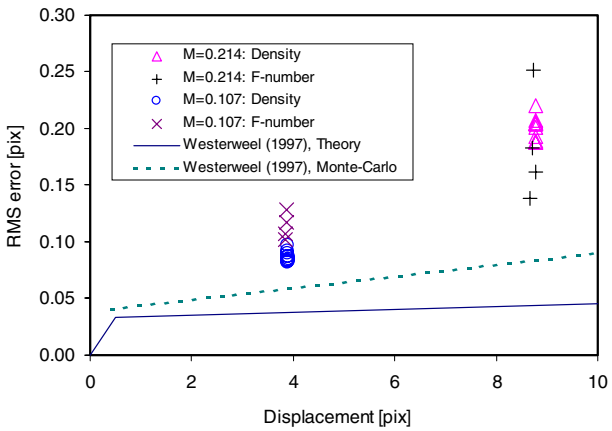

Figure 8. Absolute RMS error as a function of the mean image displacement for both magnifications. Cases for varying density as well as f-stop are given for best focus location only.

range of integer displacements were encountered covered in the experiments. Nevertheless, if it were a concern, it is expected that PDFs centred at a displacement value of 3.9 pixels were influenced at the trailing end towards four pixel displacement, but the distribution seen in figure 4 drops to a zero bin count of around 3.95.

A comparison between this data and the predictions of Westerweel (1997) is given in figures 8 and 9. Figure 8 shows the error as a function of displacement for both the theoretical predictions and Monte Carlo simulations from Westerweel

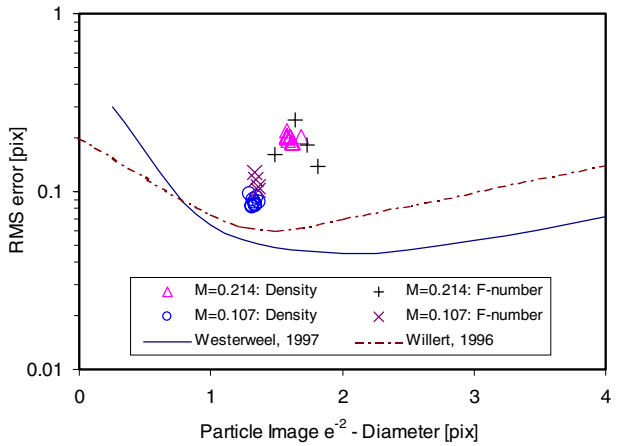

Figure 9. Absolute RMS error as a function of the mean particle image diameter for both magnifications. Cases for varying density as well as f-stop are given for the best focus location only.

(1997). The trends are consistent. Theory predicts the lowest error at zero displacement, increasing with finite values of displacement as was found by Adrian (1997) and Willert (1996). Note that all of the data was shown to reveal the range of values; the experimental data with the lowest errors are the best comparison with the predictions. The slopes between the Monte Carlo modelling results and the experimental data differ by approximately a factor of 2. The magnitude of the error at best focus is larger than the predictions, presumed to be a result of the differences between the idealized predictions and the non-ideal effects of the experimental particles and imaging systems.

Figure 9 compares the experimental data and Westerweel's (1997) theoretical predictions of the absolute RMS error (in units of pixels) as a function of the particle image size. The discrepancy between theory and experiment is within a factor of 2–4. No Monte Carlo model data were presented by Westerweel for particle image size as a parameter. Experimental data obtained by Willert (1996) shows RMS errors between our results and Westerweel's model; this is similar to the trend for RMS error as a function of displacement. Note that the model could vary particle image sizes without altering any other parameter, whereas the experimental particle image diameters resulted from parameter changes such as imaging off-focus in addition to varying magnification. It

is plausible that the increased errors associated with the experimental approach are manifold (such as decrease in particle image intensity, overlap and higher background noise). Thus larger errors can be expected in contrast to a scenario where the particle image size alone could have been changed keeping the intensity of the particle image illumination (over an enlarged area), seed density and magnification constant.

Overall, the results agree quite well with the theory and model of Westerweel (1997). The absolute displacement accuracies of the order of 0.08–0.2 pixels are about a factor of two larger than those predicted by Westerweel (1997) for a 32 by 32 pixel interrogation spot.

4. Conclusions

The accuracy and precision of digital PIV measurements were investigated, experimentally, for a range of parameters including magnification, f-stop, seeding density and focusing. It is important to emphasize that the point of this study was not to find the best obtainable measurement accuracy and precision. Rather, the purpose was to investigate the dependence of the accuracy and precision on the various practical parameters.

The investigations used electro-optical shifting of cross-polarized scattering signals of a random particle field to create an artificial, repeatable displacement field of images that originated from laser-illuminated silicone oil droplets. Double-exposure single-image cross-correlation digital PIV was used to measure the displacement fields. Magnifications, M, of 0.107 and 0.214 were selected as representative values for targeted measurements in, for example, optical IC engines yielding resolutions of 2 and 1 mm, respectively. 60 images were acquired and interrogated at each of the parameter values and ensemble averaged. The effect of the parameters on the accuracy was determined by measuring the change in the average displacement, the effect of the parameters on the precision was determined as the RMS fluctuations about the ensemble average. The change in the mean displacement (accuracy) was less than 1% which is much less than the change in the precision (RMS fluctuations).

The measured fluctuations of the droplet image displacements were found to be nearly independent of the seeding density in the range of 10–40 droplets within a 32×32 pixel interrogation window. The selection of the f-stop had a more pronounced effect for $M = 0.214$ where the RMS of the measured displacement dropped from 3% for $f/2.8$ to less than 1.5% for $f/5.6$. For $M = 0.107$ the fluctuations were found to be around 3% for all f-stops. The largest impact is found for the cases when the images were deliberately defocused, where errors up to 4% were found. Increase of particle size by means of defocusing does not improve detectability and increases the measurement error for all cases investigated. Explanations for the different sensitivity to the same off-focus recording lie in the decreased depth-of-field for the higher magnification case ($M = 0.214$) as compared to $M = 0.107$. This is mainly caused by the loss of particle image intensity and deteriorated contrast for particle image detection. It was also found that the lowest RMS fluctuations were correlated with the most symmetric PDF even if this did not coincide with the largest measured displacement. It is hypothesized that the increased errors were due to increased image aberrations caused by small $f/\#$ and defocusing.

Comparison of the RMS error obtained in this study with experimental and modelled data provided by Willert (1996) and modelled data based on theory developed by Westerweel (1997) is in good agreement qualitatively. The error in the experimental data was in general found to be by a factor of 2–4 higher than the theory or modelled data but was found to be in better agreement with experimentally obtained data (Willert 1996). Due to the limitations of the experimental approach in terms of isolating and varying parameters independently, trends described in the model could only be verified at selected points but were found to support the predictions. In particular, this data demonstrates:

(1) independence of displacement accuracy for seed density beyond a transition range,
(2) an RMS error of less than 0.1 pixels for particle image diameters between 1 and 2 pixels, and
(3) linear increase of error as a function of displacement magnitude equal to an offset between the first and second interrogation windows.

Acknowledgment

This work was supported by the General Motors Corporation within the Collaborative Research Laboratory at the University of Michigan.

References

Adrian R J 1997 Dynamic ranges of velocity and spatial resolution of particle image velocimetry *Meas. Sci. Technol.* **8** 1393–8

Keane R D and Adrian R J 1990 Optimization of particle image velocimeters Part 1: double pulsed systems *Meas. Sci. Technol.* **1** 1202–15

Landreth C C and Adrian R J 1988 Electrooptical image shifting for particle image velocimetry *Appl. Opt.* **27** 4216–20

Raffel M, Willert C and Kompenhans J 1998 *Particle Image Velocimetry—A Practical Guide* (Berlin: Springer)

Reuss D L 1993 Two-dimensional particle-image velocimetry with electrooptical image shifting in an internal combustion engine *Proc. Int. Soc. Opt. Eng. (Optical Diagnostics in Fluids and Thermal Flow vol 2005)* pp 413–24

Westerweel J 1997 Fundamentals of digital particle image velocimetry *Meas. Sci. Technol.* **8** 1379–92

Westerweel J 2000 Theoretical analysis of the measurement precision in particle image velocimetry *Exp. Fluids Suppl.* S3–S12

Willert C E 1996 The fully digital evaluation of photographic recording *Appl. Sci. Res.* **56** 79–102

Willert C E and Gharib M 1991 Digital particle image velocimetry *Exp. Fluids* **10** 181–93